Behavioral/Cognitive

Quantifying the Microvascular Origin of BOLD-fMRI from First Principles with Two-Photon Microscopy and an Oxygen-Sensitive Nanoprobe

Louis Gagnon,[1,2] Sava Sakadžić,[1] Frédéric Lesage,[3] Joseph J. Musacchia,[1] Joël Lefebvre[3], Qianqian Fang,[1] Meryem A. Yücel,[1] Karleyton C. Evans,[1] Emiri T. Mandeville,[1] Jülien Cohen-Adad,[3] Joñathan R. Polimeni,[1] Mohammad A. Yaseen,[1] Eng H. Lo,[1] Douglas N. Greve,[1] Richard B. Buxton,[5] Anders M. Dale,[4,5] Anna Devor,[1,4,5] and David A. Boas[1,2]

[1]Athinoula A. Martinos Center for Biomedical Imaging, Department of Radiology, Massachusetts General Hospital, Harvard Medical School, Charlestown, Massachusetts 02129, [2]Harvard-MIT Division of Health Sciences and Technology, Cambridge, Massachusetts 02139, [3]Department of Electrical Engineering, École Polytechnique de Montréal, Montréal, Quebec, Canada H3C 3A7, and Departments of [4]Neurosciences and [5]Radiology, UC San Diego, La Jolla, California 92093

The blood oxygenation level-dependent (BOLD) contrast is widely used in functional magnetic resonance imaging (fMRI) studies aimed at investigating neuronal activity. However, the BOLD signal reflects changes in blood volume and oxygenation rather than neuronal activity per se. Therefore, understanding the transformation of microscopic vascular behavior into macroscopic BOLD signals is at the foundation of physiologically informed noninvasive neuroimaging. Here, we use oxygen-sensitive two-photon microscopy to measure the BOLD-relevant microvascular physiology occurring within a typical rodent fMRI voxel and predict the BOLD signal from first principles using those measurements. The predictive power of the approach is illustrated by quantifying variations in the BOLD signal induced by the morphological folding of the human cortex. This framework is then used to quantify the contribution of individual vascular compartments and other factors to the BOLD signal for different magnet strengths and pulse sequences.

Key words: **BOLD-fMRI; modeling; Monte Carlo; two-photon microscopy**

Introduction

Functional magnetic resonance imaging (fMRI)-based on the blood oxygenation level-dependent (BOLD) response (Ogawa et al., 1990; Kwong et al., 1992) has become a widely used tool for exploring brain function, and yet the neurophysiological basis of this technique remains poorly understood (Logothetis, 2008; Kim and Ogawa, 2012). The BOLD signal arises from the orchestrated microscopic activity of the underlying neuronal networks but does not reflect this activity directly (Logothetis, 2008). Rather, the signal measured depends on microscopic magnetic field perturbations arising from changes in oxygenation and blood volume in the cortical microvasculature (Uludağ et al., 2009; Buxton, 2010), which are themselves driven by neurovascular coupling (i.e., changes in blood flow and oxygen consumption associated with neuronal and glial activity). By itself, understanding neurovascular coupling has been a very active area of research since the beginning of fMRI (Attwell et al., 2010). Separately, understanding the transformation of microscopic vascular dilation and oxygenation into macroscopic BOLD signals is an important step toward the physiological interpretation of BOLD (Buxton, 2010). Specifically, understanding how individual vascular compartments are reflected in the BOLD signal and quantifying volume and oxygenation effects individually for different pulse sequences and for different magnetic field strengths is critical for a physiologically informed choice of sequence parameters, for the development of new quantitative fMRI methods to measure the cerebral metabolic rate of oxygen ($CMRO_2$), for the development of high-field fMRI technologies and for the interpretation of neuroimaging data in the context of vascular diseases. Nevertheless, achieving these goals has been challenging because of the difficulty of measuring vessel geometry and blood oxygenation in individual microvascular compartments during cerebral activation. Typically, these quantities are rather assumed, which significantly reduces our accuracy to compute the individual contributions mentioned above (Buxton, 2010).

Received Aug. 25, 2014; revised Dec. 26, 2014; accepted Jan. 14, 2015.

Author contributions: L.G., S.S., F.L., Q.F., K.C.E., E.H.L., R.B.B., A.M.D., A.D., and D.A.B. designed research; L.G., S.S., F.L., Q.F., K.C.E., E.T.M., J.C.-A., J.R.P., M.A.Yücel, D.N.G., R.B., A.M.D., A.D., and D.A.B. performed research; L.G., S.S., J.J.M., J.L., M.A.Yaseen, J.C.-A., J.R.P., M.A. Yücel, D.N.G., A.M.D., A.D., and D.A.B. analyzed data; L.G., J.C.-A., J.R.P., R.B., A.D., and D.A.B. wrote the paper.

This work was supported by NIH Grants P41RR14075, R01NS057476, R00NS067050, R01NS057198, and R01EB000790, American Heart Association Grant 11SDG7600037, and the Advanced Multimodal NeuroImaging Training Program (R90DA023427 to L.G.). We thank Elfar Adalsteinsson, Jerrold Boxerman, Jean Chen, Audrey Fan, Valerie Griffeth, Sune Jesperson, David Kleinfeld, Joseph Mandeville, Leif Ostergaard, Axel Pries, Bruce Rosen, Aaron Simon, Vivek Srinivasan, Bojana Stefanovic, and Larry Wald for fruitful discussions.

The authors declare no competing financial interests.

Correspondence should be addressed to Dr Louis Gagnon, Massachusetts General Hospital, Charlestown, MA. E-mail: lgagnon@nmr.mgh.harvard.edu.

L. Gagnon's present address: Department of Electrical Engineering, École Polytechnique de Montréal, Montréal, QC, Canada H3C 3A7.

DOI:10.1523/JNEUROSCI.3555-14.2015

 0270-6474/15/353663-13$15.00/0

Here, we overcome this difficulty by taking advantage of recent advances in multiphoton microscopy (Finikova et al., 2008; Sakadzić et al., 2010; Devor et al., 2011; Lecoq et al., 2011; Parpaleix et al., 2013) to measure microvascular geometry and oxygen distribution *in vivo* in rodents, at rest and during forepaw stimulation. These physiological measurements were then used to predict the BOLD signal from first principles and our bottom-up approach was validated against experimental fMRI measurements at several levels. Accounting for the real geometry and oxygen distribution of the microvasculature, our framework allowed us to quantify the variations in the BOLD signal produced by the complex folding of the human cortex. These variations were then measured experimentally, demonstrating the predictive power of our model. Furthermore, our bottom-up approach allowed us to reverse engineer the content of the BOLD signal (i.e., quantify its phenomenological origin for different magnet strengths, pulse sequences, and sequence parameters, as well as the orientation of the cortical sheet relative to the magnetic field) directly without the need of traditional assumptions about cerebrovascular physiology.

Materials and Methods

Baseline measurements of pO_2 and angiography

All experimental procedures were approved by the Massachusetts General Hospital Subcommittee on Research Animal Care. We anesthetized C57BL/6 mice (male, 25–30 g, $n = 6$) by isoflurane (1–2% in a mixture of O_2 and air) under constant temperature (37°C). A cranial window with the dura removed was sealed with a 150-μm-thick microscope coverslip. During the experiments, we used a catheter in the femoral artery to monitor the systemic blood pressure and blood gases and to administer the two-photon dyes. During the measurement period, mice breathed a mixture of O_2, and air under the 0.7–1.2% isoflurane anesthesia. Imaging was performed using a custom built two-photon microscope (Sakadzić et al., 2010) and two-photon enhanced oxygen-sensitive phosphorescent dye PtP-C343 (Finikova et al., 2008). The time-domain measurements of phosphorescence lifetimes were performed following the procedures outlined by Sakadzić et al., (2010), Devor et al. (2011), and Parpaleix et al. (2013). Approximately 400 pO_2 measurements were collected in various microvascular segments down to 450 μm from the cortical surface. The conversion between pO_2 and oxygen saturation of hemoglobin (SO_2) was performed using the Hill equation with Hill coefficients specific for C57BL/6 mice ($h = 2.59$ and $P50 = 40.2$; Uchida et al., 1998).

After collecting the pO_2 measurements, we obtained structural images of the cortical vasculature by labeling the blood plasma with dextran-conjugated fluorescein (FITC) at 500 nM concentration. We acquired $600 \times 600 \times 662$ μm stacks of the vasculature with $1.2 \times 1.2 \times 2.0$ μm voxel sizes under a 20× Olympus objective (NA = 0.95). The baseline pO2 measurements were recently published by Sakadzić et al. (2014).

Functional measurements on rodents

Rationale for using both rats and mice. All baseline measurements were performed on mice while all functional measurements were performed on rats. Our motivation was to maximize both the quality of the data acquired and the feasibility of our analysis. On one hand, using mice for baseline measurements allowed us to take advantage of the powerful two-photon pO_2 measurement technology (Finikova et al., 2008; Sakadzić et al., 2010), which is more difficult on rats due to the larger blood pool. Moreover, the angiograms are easier to graph on mice, which is critical for our vascular anatomical network (VAN) model approach. On the other hand, using rats for functional data resulted in higher signal-to-noise ratio for the parameters measured (especially arterial dilation and BOLD-fMRI). A recent work performed a detailed topological analysis of the cortical microvasculature of rodents and concluded that the topology of cortical vessels is very similar for mice and rats (Blinder et al., 2010). This analysis strongly supports our hypothesis that rats and mice datasets can be mixed together without affecting substantially the results of our work.

Stimulus. All experimental procedures were approved by the University of California at San Diego Institutional Animal Care and Use Committee. Sprague-Dawley rats (130–200 g) were anesthetized as described previously (Devor et al., 2007, 2008). The stimulation lasted 2 s and consisted of a train of six electrical pulses (3 Hz, 300 μs, 1 mA) with an interstimulus interval of 20–25 s. The intensity was adjusted to provide stimulation below the movement threshold. Stimulation was presented using a separate computer that also acquired transistor–transistor logic (TTL) timing signals for data acquisition ("trigger out" TTLs for each line or frame during two-photon acquisition and for each slice during fMRI) using a National Instruments IO DAQ interface controlled by a home-written software in MATLAB. The TTL data were used to determine the timing of each line/frame/slice relative to the stimulus onset during data analysis performed in MATLAB.

Two-photon measurements of arterial dilation. Two-photon microscopy was performed on rats ($n = 19$) as described by Devor et al. (2008). Fluorescein-conjugated dextran (FD-2000; Sigma-Aldrich) in physiological saline was injected intravenously (Nishimura et al., 2006). Images were obtained with an Ultima two-photon microscopy system from Prairie Technologies using 4× (Olympus XLFluor4X/340, NA = 0.28) and 40× (Olympus, NA = 0.8) objectives. Line scans up to 1 mm long were acquired across multiple vessels (up to 6) with a scan rate of 80–170 Hz. The pixel resolution was 0.5 μm or less. Diving arterioles were measured in the frame mode at 5–8 frames/s. These measurements were previously published (Tian et al., 2010).

Confocal measurements of pO_2. Confocal microscopy was performed on rats ($n = 10$) as described by Yaseen et al. (2011). A solution of Oxyphor R2 dye (Oxygen Enterprises) in saline was administered through the femoral vein to yield a concentration of 40 μmol/L in the bloodstream. At each location, phosphorescence was excited for 100 ms. The resultant phosphorescence emission decay profile was collected at 50 MHz sampling rate for 500 ms. Fifty decay profiles were averaged for each measurement (~30 ms per point measurement). The decay lifetime was calculated and converted to pO_2 (Sakadzić et al., 2009). The temporal resolution was 0.5–1 s depending on the number of points measured per interval. These measurements were previously published (Yaseen et al., 2011).

fMRI. MRI was performed on rats ($n = 10$) on a 7T/21 cm BioSpec 70/30 USR horizontal bore scanner (Bruker) as described previously (Tian et al., 2010). BOLD functional data were acquired using a single-shot gradient-echo echo planar imaging pulse sequence with the following parameters: TE = 10 ms, flip angle = 30°, matrix = 80 × 80, slice thickness = 1 mm, TR = 1 s, five adjacent slices. The data and the laminar analysis procedure used was previously published (Tian et al., 2010).

Graphing and meshing the angiograms

To estimate vessel diameters, to label vessel types and to compute statistics across the angiogram, such as branching order from pial vessels, a mathematical representation of the vasculature must be obtained. This mathematical representation is termed a graph and consists of nodes interconnected by segments.

Structural images based on FITC-labeled blood plasma were used to construct a graph of the microvascular network for each animal. A $3 \times 3 \times 3$ median filter was used to enhance vessel contrast. We created the graphs and performed image processing using a suite of custom-designed tools in MATLAB (MathWorks). Initial steps involved running the VIDA suite (Tsai et al., 2009). The graphs were then inspected and manual corrections were applied until all segments in the field of view become interconnected (single group). Vessel diameter was estimated at each graph node by thresholding the image at a low value of ~2% of the maximum image intensity, considering lines through the node point oriented every 3° in the local plane perpendicular to the vessel axis, and finding the minimum distance from vessel edge to vessel edge (Fang et al., 2008).

A three-dimensional mask of the vasculature was obtained from the angiogram and the graph and a mesh of the vasculature was generated using the software *iso2mesh* (Fang and Boas, 2009).

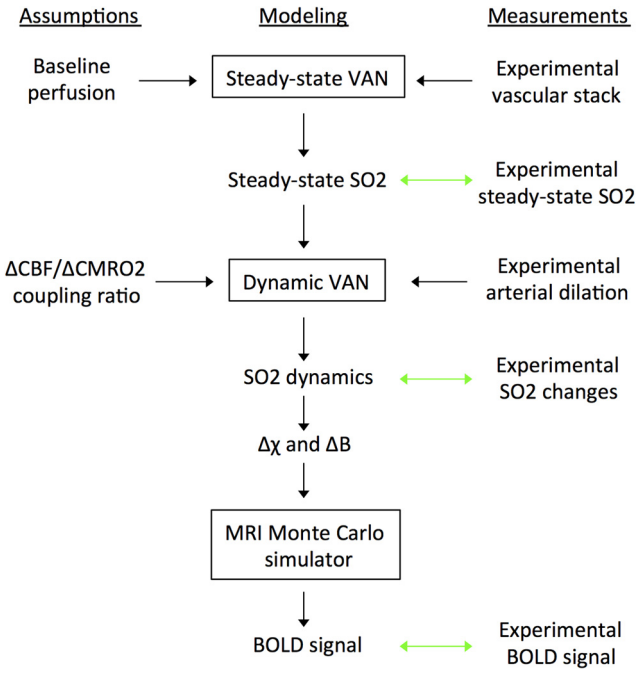

Figure 1. Overview of the modeling framework. Green arrows represent validations of the model against experimental measurements.

Vessel-type identification

Arterioles and venules were labeled manually by following them from the pial surface into the cortical depth. The identification of the pial arterioles and venules was done based on pO_2 measurements and their morphology, where surface pial arteries tend to be straighter, thinner, and gradually branching into smaller vessels, and can be easily distinguished from surface pial veins, which are more curvy, thicker, and branching into vessels of all calibers. Capillaries were typically identified a few branches away from the diving arterioles based on their diameter ($\leq$8 μm) and morphology. The Floyd–Warshall algorithm was then used to calculate branching orders of individual vascular segments with respect to main pial vessels, which were manually identified.

Vascular anatomical network model

Rationale. The complete set of measurements required to acquire the angiogram and the pO_2 distribution at rest takes ~45 min. It was therefore not possible to measure all vessel sizes and the entire pO_2 distribution at every time point during functional activation with short stimulus, which are the typical stimulus length used in human event-related fMRI experiments. To model the BOLD signal accurately, we aimed at reconstructing changes in vessel size and oxygenation with a temporal resolution of ~1 s, which is 3 orders of magnitude faster than what the current technology can achieve. To overcome this limitation, we instead focused on measuring a single parameter at a time (i.e., vessel diameters or pO_2 changes) during functional activation. Together with a VAN model, these functional measurements allowed us to reconstruct oxygenation changes in all vessel segments contained in the field-of-view (600 $\times$ 600 $\times$ 662 μm) with very good temporal resolution (~0.1 s), which was not achievable with the actual microscope technology alone.

Overview. An overview of the entire modeling procedure is illustrated in Figure 1. Vessel dilation in the arterial compartment is an active process mediated by the release of vasodilatory agents and therefore these measurements were used as inputs to perturb the VAN model from steady-state during functional activation. Flow changes and volume changes can then be computed in all vascular segments assuming a passive compliance model for the capillary and the venous bed. Knowing the flow and volume changes allowed us to compute the changes in oxygenation in all the vessels assuming a $\Delta Flow/\Delta CMRO_2$ coupling ratio. To ensure the accuracy and realism of this approach, the simulated oxygenation changes were then compared with partial pO_2 measurements during functional activation. For all six vascular networks constructed, this approach gave very good agreement between the simulated and the measured functional changes.

Table 1. Physiological parameters for mice

ID	p_aO_2 (mmHg)	p_vO_2 (mmHg)	s_aO_2 (%)	s_vO_2 (%)	OEF (%)	$CMRO_2$ (μmol/ml/min)
1	109	44	92	58	36.9	2.28
2	94	43	88	54	38.6	2.32
3	107	60	93	67	28.0	1.72
4	116	57	93	66	29.0	1.81
5	118	60	94	68	27.7	1.73
6	109	41	91	58	36.2	2.23
Mean	108.8	50.8	91.8	61.8	32.7	2.02
SD	8.5	9.1	2.1	5.9	5.0	0.26

Steady-state VAN. The goal here was to reconstruct the resting distribution of oxygen in all vessels. This distribution was then compared with the pO_2 distribution measured experimentally to confirm its realism. This steady-state distribution was then perturbed during functional activation.

The oxygenation level in the vasculature was globally determined by two competing parameters, which are blood flow and the cerebral metabolic rate of oxygen ($CMRO_2$). Higher blood flow increases oxygenation while higher $CMRO_2$ decreases it. In steady-state, these two parameters are related by the following:

$$CMRO_2 = CBF \times OEF \times C_a, \quad (1)$$

where OEF is the oxygen extraction fraction and C_a is the arterial blood oxygen content given by the following:

$$C_a = p_aO_2\alpha + 4HctC_{Hb}S_aO_2, \quad (2)$$

where $\alpha = 1.27 \times 10^{-3}$ μmol/ml/mmHg is the solubility of oxygen, $C_{Hb} = 5.3$ μmol/ml is the hemoglobin content of blood and Hct = 0.4 is the hematocrit in arteries. OEF was computed directly for each animal using our two-photon measurements as follows:

$$OEF = \frac{S_aO_2 - S_vO_2}{S_aO_2}. \quad (3)$$

Baseline CBF in rodents has been previously measured with positron emission tomography (PET) and fMRI, and is well documented in the literature (Wehrl et al., 2010; Zheng et al., 2010). Wehrl et al. (2010) reported a value of 75 ml/100 g/min over the cortex using PET, whereas Zheng et al. (2010) reported a value of 125 ml/100 g/min with a 15% variation over the cortex using fMRI. We therefore fixed CBF to obtain a perfusion of 100 ml/100 g/min in our volumes. $CMRO_2$ was then computed for each animal using Equation 1, and values obtained for each animal are shown in Table 1.

Capillary segments cut by the limits of the field-of-view were removed to obtain a closed graph between the pial arteries and the pial veins. This procedure was previously used by (Lorthois et al., 2011a,b) and was shown to result in accurate flow distributions.

The resistance for each segment was calculated using Poiseuille's law corrected for hematocrit as described by Pries et al. (1990). Flow speeds in inflowing pial arteries were calculated based on the perfusion assumed (100 ml/100 g/min) and the arterial diameters. Blood pressure boundary conditions for pial veins were set using values from (Lipowsky, 2005) and the blood flow distribution was finally computed using the matrix equations given by Boas et al. (2008), together with velocity boundary conditions for inflowing arteries and the blood pressure boundary conditions for outflowing veins. The arterial pressures calculated with this method agreed with the experimental arterial pressures reported by Lipowsky (2005).

Finite-element oxygen advection was then performed individually for each animal using the computed blood flow distribution and the inflowing arterial pO_2 given in Table 1 for each animal. The pO_2 was initialized everywhere to 10 mmHg and oxygen advection was run with constant inputs (including uniform $CMRO_2$ across the extravascular space) until

steady-state was achieved (typically after 15 s in the model time). The details of the finite element algorithm used can be found in our previous paper (Fang et al., 2008).

VAN model during functional activation. The arterial dilation traces were used as inputs to compute changes in blood flow and blood volume as described by Boas et al. (2008). An intracranial pressure of 10 mmHg was assumed and the compliance parameter β was set to 1 for both capillaries and veins (Boas et al., 2008).

Oxygenation changes during functional activation was then computed using the same advection code (Fang et al., 2008) by keeping pO_2 in the arterial inflowing nodes constant and using the updated flow and volume values at each time point. $CMRO_2$ was increased following a temporal profile corresponding the averaged arterial dilation trace with a peak amplitude corresponding to a relative change three times lower compared with the relative change in blood flow, giving a $\Delta Flow/\Delta CMRO_2$ coupling ratio of 3 (Huppert et al., 2007; Dubeau et al., 2011).

fMRI simulations

Overview. The BOLD signal is a measure of the transverse magnetization of nuclear spins. In gradient echo (GRE) BOLD, two processes contribute to the decay of the signal: dipole-dipole coupling (spin-spin interactions), as well as dephasing induced by microscopic and macroscopic field inhomogeneities in the local magnetic field (Yablonskiy and Haacke, 1994). The relaxation constant embedding these two processes is termed $T_2^\star$. In spin echo (SE) BOLD, the effect of field inhomogeneities is reversed around larger vessels (veins) using a 180° refocusing pulse. The relaxation constant in this case is termed T_2. A contributor to the local magnetic field inhomogeneities is the presence of deoxyhemoglobin in the vasculature, which is paramagnetic. During functional activation, variations in vessel size and oxygenation level affect the geometry and the amplitude of these magnetic field inhomogeneities and therefore affect $T_2^\star$. Furthermore, the oxygenation level affects spin–spin coupling and therefore T_2.

The challenges in modeling BOLD are: (1) to compute the magnetic field inhomogeneities at every time point and (2) to keep track of spin-spin decay (T_2 effect). These tasks require exact knowledge of the microvascular geometry and the deoxyhemoglobin content in each vessel segment at every time point.

Computing magnetic field inhomogeneities. We used a numerical method previously described (Koch et al., 2006; Pathak et al., 2008) to compute the magnetic field inhomogeneities. The SO_2 volumes were resampled to $1 \times 1 \times 1$ μm and converted to a susceptibility shift volume $\Delta\chi$ using the following:

$$\Delta\chi = \Delta\chi_0 Hct(1 - SO_2), \tag{4}$$

where $\Delta\chi_0 = 4\pi \cdot 0.264 \times 10^{-6}$ is the susceptibility difference between fully oxygenated and fully deoxygenated hemoglobin (Christen et al., 2011) and *Hct* is the hematocrit that was assumed to be 0.3 in capillaries and 0.4 in arteries and veins (Griffeth and Buxton, 2011).

Assuming that the magnetic field inhomogeneities are small, the method uses perturbation theory and the inhomogeneities across the entire volume are computed by convolving the susceptibility shift volume $\Delta\chi$ with the geometrical factor for the magnetic field inhomogeneity induced by a unit cube as follows:

$$\Delta B_{cube} = \left(\frac{6}{\pi}\right)\frac{1}{3}\frac{a^3}{r^3}(3\cos^2\theta - 1)B_0, \tag{5}$$

where a represents the grid size (1 μm) and r and θ are the polar coordinates. This procedure allowed computation of the magnetic field inhomogeneities across the entire vascular volume $\delta B_{\text{inhom}}(x)$.

T_2 and $T_2^\star$ volumes. In addition to magnetic field inhomogeneity, T_2 and $T_2^\star$ volumes are required to accurately model the fMRI signals. T_2 and $T_2^\star$ values (in seconds) along the vasculature were computed using the formulas obtained by fitting experimental measurements and given in as follows (Uludağ et al., 2009):

$$T_{2,\text{vessel}} = (12.67B_0^2(1 - SO_2)^2 + 2.74B_0 - 0.6)^{-1}, \tag{6}$$

Table 2. Empirical constants for T_2* of blood

$B_0 \leq 1.5$T	A = 6.5	C = 25
1.5T $< B_0 \leq$ 3T	A = 13.8	C = 181
3T $< B_0 \leq$ 4T	A = 30.4	C = 262
4T $< B_0 \leq$ 4.7T	A = 41	C = 319
$B_0 >$ 4.7T	A = 100	C = 500

$$T^*_{2,\text{vessel}} = (A + C(1 - SO_2)^2)^{-1}, \tag{7}$$

where A and C are constants (in seconds^{-1}) which depend on the external magnetic field B_0 and given in Table 2.

In the tissue (outside the vessels), T_2 and $T_2^\star$ (in seconds) were computed using the formulas given as follows (Uludağ et al., 2009):

$$T_{2,\text{tissue}} = (1.74B_0 + 7.77)^{-1}, \tag{8}$$

$$T^*_{2,\text{vessel}} = (3.74B_0 + 9.77)^{-1}. \tag{9}$$

Monte Carlo simulation of nuclear spins. Water protons experience diffusion in cortical tissue, which was simulated with Monte Carlo simulations (Boxerman et al., 1995a; Martindale et al., 2008). The positions of 10^7 protons were initialized uniformly in the three-dimensional volume. Each proton experienced a random walk for a period of TE sec. The diffusion coefficient was set to 1×10^{-5} cm^2/s (Pathak et al., 2008) and the time step dt was set to 0.2×10^{-3} sec. At each time step, the position $x = (x_1\ x_2\ x_3)$ of each proton was updated using

$$x_1' = x_1 + N(0,\ 2Ddt), \tag{10}$$

$$x_1' = x_2 + N(0,\ 2Ddt), \tag{11}$$

$$x_1' = x_3 + N(0,\ 2Ddt). \tag{12}$$

Protons reaching a vessel wall were bounced back, such that all protons stayed outside the vessels for the duration of the simulation. The MR signal was computed at each time step by averaging the contribution of all N protons as follows:

$$S(t) = Re\left\{\frac{1}{N}\sum_{i=1}^{N} e^{\varphi_n(t)}\right\}, \tag{13}$$

where the generalized phase (including both precession and relaxation) was updated every time step using:

$$\phi_{n,\text{extra}}(t) = \sum_{k=1}^{t/dt} \gamma j \Delta B(x(k)) - T_{2,\text{tissue}}(x(k)), \tag{14}$$

where γ is the hydrogen proton precession frequency, j the imaginary unit, and:

$$\Delta B(x(k)) = \Delta B_{\text{inhom}}(x(k)) + \Delta B_{\text{gradients}}(x(k)), \tag{15}$$

with ΔB_{inhom} the magnetic field homogeneity computed above and $\Delta B_{\text{gradients}}$ is the field homogeneity introduced by the spatial gradient. For SE signal, the imaginary part of the phase was inverted at TE/2

$$\phi_n(TE/2) = \text{conj}(\phi_n(TE/2)). \tag{16}$$

We note that only the extravascular protons were modeled, which constitute the dominant source of the signal at high fields (Uludağ et al., 2009). This method was adopted since there is no current microscopic way of modeling accurately the intravascular signal. The numerical method produces relatively uniform magnetic fields inside the vasculature, while in reality there are very strong dipolar fields arising around red blood cells that are tumbling around and water molecules are exchanged between red blood cells and the plasma.

This procedure is repeated at each desired time point during the functional activation. The relative signal changes was computed by comparing the signal obtained at each time point to the signal obtained at $t = 0$ and converted to a percentage change.

Calculation of the angular dependence of BOLD

To quantify the angular dependence of the BOLD response, we compared the BOLD signal changes simulated at different θ_z values with the BOLD signal changes simulated at $\theta_z = 0°$. The difference was converted to a percentage with respect to $\theta_z = 90°$, as follows:

$$\mathrm{diff}\,(\theta_z) = 100 \times \frac{\Delta S_{\theta_z} - \Delta S_{\theta_{z=90°}}}{\Delta S_{\theta_{z=90°}}}. \quad (17)$$

With this definition, a variation of 40% indicates that the BOLD signal change for $\theta_z = 0°$ is 40% stronger compared with the BOLD signal change for $\theta_z = 90°$.

Experimental BOLD measurements on human

BOLD during hypercapnia. All experimental procedures were approved by the Massachusetts General Hospital. Healthy subjects ($n = 5$) were enrolled in the study. Written consent was received from each subject before the experiment. During fMRI scanning, subjects breathed through a SCUBA-like mouth-piece attached to a specialized breathing circuit that enabled steady-state levels of end-tidal pCO_2 (Banzett et al., 2000). The end-tidal pCO_2 was measured at the mouthpiece continuously during each fMRI scan via MRI-compatible capnograph (Capstar-100, CWE) to verify the target levels of end-tidal pCO_2. Hypercapnia was achieved by adding CO_2 to the inspirate. Each subject received two 2 min blocks hypercapnia during which end-tidal pCO_2 was maintained at a level of 8 mmHg above the subject's baseline pCO_2 value. The hypercapnic blocks were interleaved with 3 min blocks at baseline pCO_2 (normocapnia).

Combined ASL-BOLD data were collected simultaneously at 3T during the gas manipulations. BOLD images were extracted from the time series and corresponded to the control images. Sequence parameters were TR = 3000 ms, IR-1 = 600 ms, IR-2 = 1800 ms, TE = 13 ms, flip angle = 90°, Res = 3.4 × 3.4 × 6.0 mm, 6 slices. An anatomical T1-weighted scan (MPRage) was also collected (Res = 1 × 1 × 1.2 mm). These measurements were previously published (Yücel et al., 2014).

Angular analysis. BOLD data were analyzed using Freesurfer. Motion correction and slice-timing correction were applied. No smoothing was used. BOLD signal changes between normocapnic and hypercapnic conditions were computed across the six slices.

A complete cortical surface reconstruction of the anatomical scan was performed with Freesurfer using the *recon-all* function. An additional cortical surface was generated midway in the gray matter and the angle between the normal to this surface and B_0 was computed as previously described (Cohen-Adad et al., 2012). The BOLD signal volumes were then interpolated on this surface, leading to a series of voxels containing both θ_z and BOLD change values. The data were pruned by selecting only voxel with a BOLD response between 0% and +10%. Voxels with BOLD response larger than 10% were probably located inside large pial vessels and did not contain cortical tissue. These voxels were therefore rejected from the analysis. Voxels with negative BOLD responses were potentially strongly contaminated with noise and were also rejected from the analysis.

The pruned data point were binned based on θ_z at every four degrees between 0° and 180° and the average BOLD change for each bin was computed. The variation in BOLD change with respect to BOLD change at $\theta_z = 90°$ was computed using Eq. 17.

Individual contributions to the BOLD signal

The individual contributions to the BOLD signal were computed at the peak of the activation, which occurred between 3.5 and 4 s (depending on the animal) after the start of the stimulus. For each field strength, TE was set to $T^*_{2,\mathrm{tissue}}$ for GRE and to $T_{2,\ \mathrm{tissue}}$ for SE as shown in the Table 3.

Arteries, capillaries, and veins contributions. To compute the contribution of an individual vascular compartment (e.g., the capillaries), two different simulations were performed. In the first one, the oxygenation volume (with dilated vessels) computed with the VAN at the peak of the functional activation was used. The signal obtained (termed total BOLD response) was compared with the signal obtained using the oxygenation volume (with baseline vessel size) at $t = 0$. In the second simulation, we constructed a new volume by using baseline (values at $t = 0$) oxygenation and vessel size for arteries and veins, but peak values for oxygenation and vessel sizes for capillaries. The signal obtained (termed capillary BOLD signal change) in this case was also compared with the same baseline signal computed using baseline oxygenation and vessel size everywhere. To compute the individual contribution of the capillaries, the capillary BOLD signal change was divided by the total BOLD signal change and converted to percentage. This procedure was repeated for arteries and veins, and for all field strengths.

Blood volume changes and oxygenation changes contributions. To compute the contribution of cerebral blood volume (CBV) changes, two simulations were performed. In the first one, both the oxygenation changes and vessel diameter changes given from the VAN models were taken into account. In the second one, only the oxygenation changes were taken into account, whereas the vessel diameters were kept constant. The net CBV contribution was computed as the difference between the standard and the oxygenation only signals normalized to the standard signal (in percentage). A negative CBV contribution indicates that the BOLD signal produced would be higher with no vessel dilation (only oxygenation changes). The negative CBV contribution occurs because dilation of vessels containing deoxyhemoglobin increase the total amount of deoxyhemoglobin in a given fMRI voxel which reduces the signal measured.

Table 3. T_2* and T_2 values for tissue at different *B* fields

Field (T)	$T^*_{2,\mathrm{tissue}}$ (ms)	$T_{2,\mathrm{tissue}}$ (ms)
1.5	65	96
3.0	48	77
4.7	37	62
7.0	28	50
9.4	22	41
11.7	19	35
14.0	16	31

Results

Reconstruction of realistic vascular networks and baseline oxygen distribution

To reconstruct baseline oxygen distribution across real vascular networks, two-photon microscopy was performed first on a set of anesthetized mice ($n = 6$) as described in Materials and Methods. Briefly, an intravascular oxygen-sensitive nanoprobe (PtP-C343) was injected for the pO_2 measurements followed by the injection of FITC for angiography. The angiogram for a representative animal is shown in Figure 2*A*. Unfortunately, the power of this technology can only be exploited on rodents. Although it is known that the arteries/veins ratio varies between rodents and primates (Hirsch et al., 2012), it is assumed here that the oxygen distribution along the different microvascular compartments of the cortex is similar between rodents and humans. With this assumption, modeling the BOLD signal over real rodent data represent a significant improvement over previous models based on random cylinder distributions (Boxerman et al., 1995b; Uludağ et al., 2009) or uniform oxygen distributions (Christen et al., 2011).

To reconstruct microvascular oxygenation with sufficient spatiotemporal resolution to accurately model the BOLD signal in each animal ($n = 6$), six VAN models were created (i.e., one for each animal; Fang et al., 2008; Blinder et al., 2013; see Materials and Methods). Angiograms were graphed using a suite of custom-built computer programs (Fang et al., 2008; Tsai et al., 2009) and a mesh of the vasculature was then created (Fang et al., 2008). Each vessel segment was identified as an artery, a capillary or a vein as shown in Figure 2*B*. The blood flow distribution (Fig. 2*C*) was obtained for each animal after computing the resistance of all vascular segments on each graph and assuming global perfusion (see Materials and Methods). For this purpose, capillary segments cut by the limits of the field-of-view were removed to obtain a closed graph between the pial arteries and the pial veins.

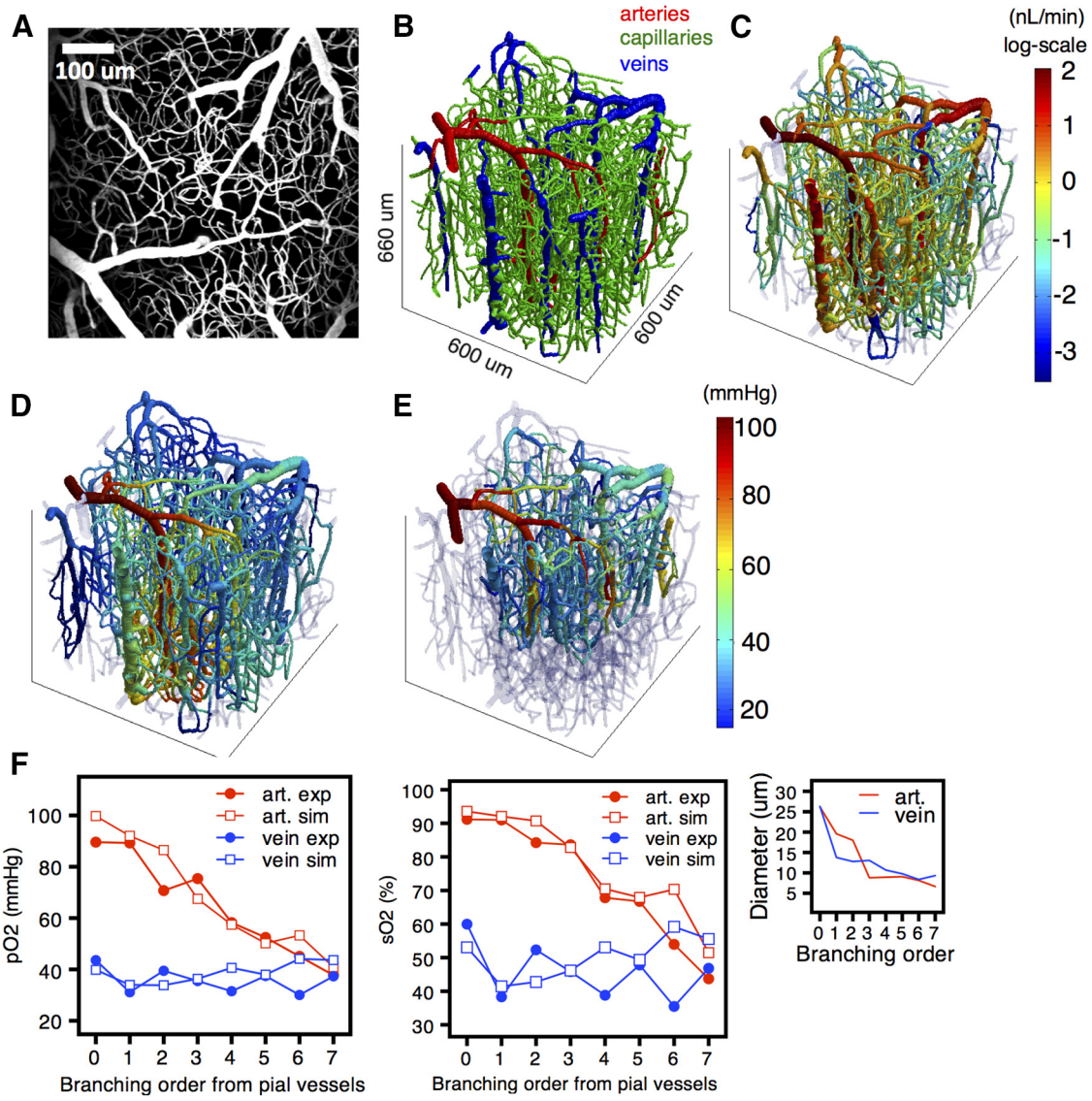

Figure 2. Construction of realistic vascular networks. ***A***, TPM FITC angiogram of the mouse cortex. ***B***, FEM mesh of the vasculature displaying arteries, capillaries, and veins. ***C***, Blood flow distribution simulated across the vascular network assuming a global perfusion value of 100 ml/min/100 g. ***D***, Distribution of the partial pressure of oxygen (pO_2) simulated across the vascular network using the finite element method model. ***E***, TPM experimental measurements of pO_2 *in vivo* using PtP-C343 dye. ***F***, Quantitative comparison of simulated and experimental pO_2 and SO_2 distributions across the vascular network for a single animal. Traces represent arterioles and capillaries (red) and venules and capillaries (blue) as a function of the branching order from pial arterioles and venules, respectively.

This procedure was previously used by Lorthois et al., (2011a,b) and was shown to result in accurate flow distributions. OEF was obtained from the experimental pO_2 measurements for each animal, and $CMRO_2$ was derived in each case from OEF and blood flow. Given blood flow and $CMRO_2$, the oxygen distribution was simulated for each VAN model by using the experimental pO_2 measurements as boundary conditions and using a finite element approach (Fang et al., 2008). A typical distribution of pO_2 obtained is shown in Figure 2*D* and compared against the experimental pO_2 measurements in Figure 2*E*. The agreement between the simulated and the experimental pO_2 measurements is demonstrated in Figure 2*F*, where both pO_2 and SO_2 are compared as a function of branching order from pial vessels for this animal.

Reconstruction of the physiological response to forepaw stimulation

The stimulus used for our functional measurements was a 2-s-long electrical stimulation of the forepaw. The dilation of the vasculature following the stimulus was measured on a separated set of anesthetized rats ($n = 19$) using two-photon microscopy as previously described (Devor et al., 2008; Tian et al., 2010; see Materials and Methods). Time courses of the dilation were averaged for the surface pial arteries, the arterial diving trunk as well for the first and second branching precapillary arterioles (Fig. 3*A*). These time courses were used as inputs to each of the six VAN models to compute the resulting changes in flow and volume across the entire networks. An example of averaged flow changes and volume changes (both relative to baseline) for individual compartments are shown in Figures 3*B* and 2*C*, respectively, for one animal. No venous dilation was observed in our two-photon measurements, consistent with other studies involving a cranial window (Hillman et al., 2007; Lindvere et al., 2013). However, the pressure changes computed from the VAN models produced passive venous dilations of 1–2% that were further used in the fMRI model. This passive venous dilation is consistent with two-photon measurements during short stimulus (Drew et

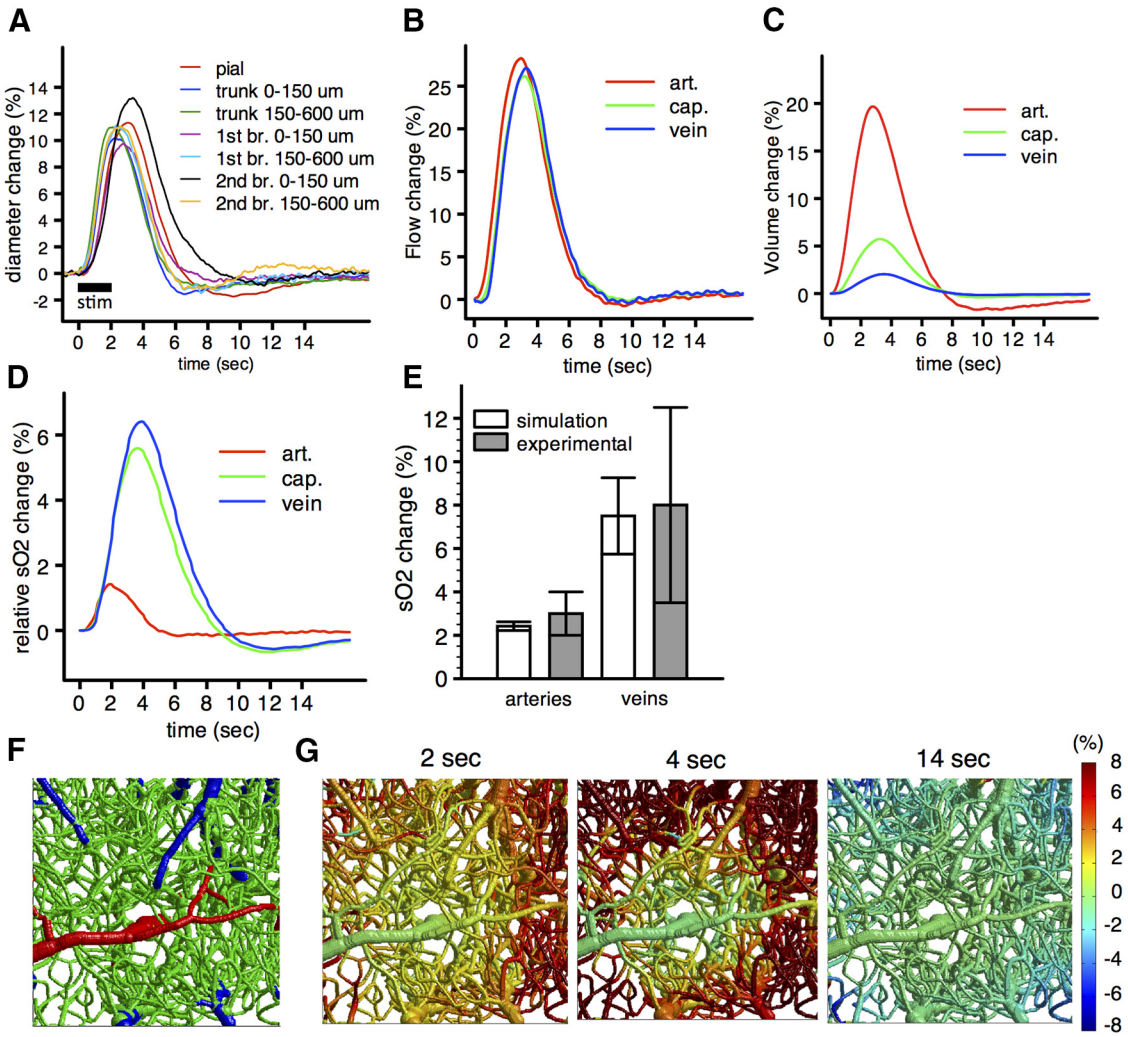

Figure 3. Modeling the physiological response to forepaw stimulus. ***A***, TPM experimental measurements or arterial dilation following forepaw stimulus. ***B***, Simulated flow changes, (***C***) simulated volume changes, and (***D***) simulated SO_2 changes (all relative to baseline) in the different vascular compartments. ***E***, Comparison of simulated SO_2 changes ($n = 6$ animals) with experimental SO_2 changes ($n = 10$ animals) measured in pial vessels during a forepaw stimulus with confocal microscopy. ***F***, Vessel type. ***G***, Spatiotemporal evolution of simulated SO_2 changes following forepaw stimulus.

al., 2011) under a reinforced thinned skull window (Drew et al., 2010), which could potentially produce a picture of activation closer to the one occurring in noninvasive human fMRI studies.

Given changes in flow and volume, we computed changes in oxygen saturation for the six VAN models assuming a ΔFlow/$\Delta CMRO_2$ ratio of 3, which is the typical value measured in rodents for short stimulations (Huppert et al., 2007; Dubeau et al., 2011). Simulated SO_2 changes for a single animal are shown in Figure 3*D* for different vascular compartments. For validation, SO_2 measurements during functional stimulation were performed in pial vessels with confocal microscopy on a separate set of rats ($n = 10$) under the same experimental conditions (Yaseen et al., 2011). A good agreement between the simulations and the experimental measurements was obtained for both arteries and veins as demonstrated in Figure 3*E*, where the average is taken across all six animals for the simulations and all 10 animals for the experimental values. These results validate our initial assumption of a blood flow change three times larger than the $CMRO_2$ change and demonstrate the realism of our VAN modeling approach. An example of changes in SO_2 across the entire vasculature (Fig. 3*F*) is shown at different time points following the forepaw stimulus in Figure 3*G*.

Modeling fMRI signals from first principles

The BOLD signal is a measure of the transverse magnetization of nuclear spins. In GRE BOLD, the signal decays to zero due to spin–spin interactions, as well as dephasing induced by magnetic field inhomogeneities. In SE BOLD, most of the later process is reversed using a 180° refocusing pulse. The presence of deoxyhemoglobin in the vasculature gives rise to microscopic magnetic field perturbations within the cortical tissue (upon its introduction in the strong field of the MR scanner) and therefore contributes to local magnetic field inhomogeneities. During increased neuronal activity, variations in vessel size and oxygenation level affect the geometry and the amplitude of these magnetic field inhomogeneities and therefore affect the GRE signal. The oxygenation level in the vessels also affects spin–spin coupling and therefore the SE signal.

Requirements to model the BOLD signal from first principles (diffusion of water molecules through the distorted magnetic field created by the deoxyhemoglobin distribution) are the knowledge of the exact geometry and size of the cerebral microvasculature, as well as the deoxyhemoglobin content in these microvessels. The difficulty in measuring these two quantities has

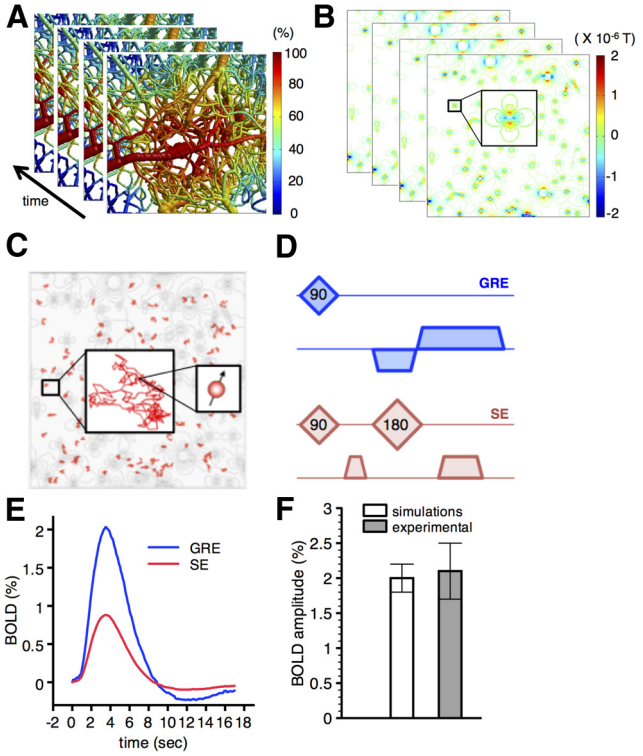

Figure 4. Modeling the fMRI signals from realistic vascular networks. ***A***, Time series of SO_2 volumes. ***B***, Resulting time series of magnetic field perturbation volumes (contour lines) computed from the SO_2 volumes at each time instant. ***C***, Simulation of nuclear spins ($n = 10^7$) diffusing in the magnetic field perturbation volume. ***D***, Spatial gradients applied to simulate GRE and SE signals. ***E***, Time series of the simulated extravascular GRE and SE signals. ***F***, Comparison of simulated GRE signal against experimental GRE signal measured during the same forepaw stimulus.

led researchers to use alternative approaches including simplifying the geometry of the vessel network with straight cylinders (Boxerman et al., 1995a; Martindale et al., 2008), simplifying the oxygen distribution in the microvasculature to uniform SO_2 (Pathak et al., 2008; Christen et al., 2011), or to use top-down models (Yablonskiy and Haacke, 1994; Davis et al., 1998; Uludağ et al., 2009). The VAN modeling approach presented here provides accurate two-photon measurements of the relevant physiological quantities, vessel geometry and oxygen content; and therefore, presents a unique opportunity to model the BOLD signal with a high level of detail and accuracy.

To predict the BOLD response from our VAN models, the magnetic field inhomogeneities were calculated for each animal from the SO_2 volumes at each time point using a numerical perturbative method (Pathak et al., 2008; Christen et al., 2011). An example of SO_2 volume and the resulting magnetic field inhomogeneities are shown in Figures 4*A* and 3*B*, respectively. BOLD was computed by simulating the random walk of proton spins within these volumes as shown in Figure 4*C* and accounting for irreversible spin-spin dephasing (see Materials and Methods). A caveat of this approach is that the perturbative method produces relatively uniform fields inside the vasculature, which is not the case in reality as strong dipole fields arise around red blood cells that are tumbling around. Therefore, we focused solely on extravascular (EV) protons here which constitute the dominant source of the signal at 3T and higher fields (Uludağ et al., 2009). Both GRE and SE signals were computed by simulating different sets of spatial gradients as illustrated in Figure 4*D*. An example of simulated GRE and SE BOLD are shown in Figure 4*E* for a single animal ($B_0 = 7$T, TE = 10 ms). Typical features of the BOLD signal can be appreciated including a large overshoot followed by a poststimulus undershoot due to a poststimulus arterial constriction (Fig. 3*A*). To test the accuracy of our simulations, we performed experimental BOLD measurements ($B_0 = 7$T, TE = 10 ms) on a separate set of rats ($n = 6$) during the same forepaw stimulations (Tian et al., 2010). For the simulations traces presented in Figure 3*E*,*F*, the direction of the external magnetic field B_0 (7T) was set perpendicular (90°) to the *z*-axis. This configuration reflects the B_0 amplitude and direction of our experimental BOLD data, which were collected with a 7T horizontal bore magnet, leading to a 90° angle between B_0 and the cortical surface of the forepaw area. The experimental data presented in Figure 4*F* are averaged over the first 600 μm of the cortex (first three slices as described previously; Tian et al., 2010) to match the volume sampled in our Monte Carlo simulations (layers I–IV). The agreement between the simulated and the experimental BOLD responses is demonstrated in Figure 4*F*, where the amplitude of the simulated signal averaged across the six VAN models is compared against the amplitude of the averaged experimental BOLD signal. The simulated EV-BOLD is slightly weaker than the experimental BOLD which is consistent with a very small additional intravascular contribution at 7T (Uludağ et al., 2009).

Local folding of the cortex produces variations in BOLD signal up to 40%

The convoluted folding of the human cortex gives rise to a wide distribution of angles between the cortical surface and the external magnetic field of the MRI scanner (Cohen-Adad et al., 2012). These angle variations are expected to affect the BOLD signal generated by the microvascular changes (Turner, 2002) but the amplitude of those variations have never been quantified. Previous works assumed isotropic or quasi-isotropic angular vessel distributions (Boxerman et al., 1995a; Martindale et al., 2008; Uludağ et al., 2009), and were therefore insensitive to this potential confounding factor. The detailed BOLD model presented here exploits measurements of the real microvascular geometry and therefore allows us to investigate the effect of the orientation of the external magnetic field of the scanner with respect to the cortical surface. For each of the six VAN models, we simulated the BOLD response by varying the orientation of the external magnetic field as shown in Figure 5*A*. The amplitude of the responses normalized in percentage change to the amplitude at $\theta_z = 90°$ is shown in Figure 5*B* for both GRE and SE ($B_0 = 3$T, TE = 13 ms). A variation of 40% was predicted from $\theta_z = 0°$ relative to $\theta_z = 90°$ for GRE, whereas little variation was observed for SE. Increasing TE from 13 to 30 ms slightly decreased this variation from 40 to 37%. This angular dependence for GRE ($TE = T_{2,\,tissue}^{*}$) varied from 35 to 60% depending on B_0 as shown in Figure 5*C*.

To confirm this prediction, simultaneous BOLD-ASL fMRI ($B_0 = 3$T, TE = 13 ms) was measured in humans ($n = 5$) during a hypercapnic challenge which would be expected to produce a relatively uniform change in deoxygenated hemoglobin in the cortex at scales where θ_z varies significantly (Wise et al., 2004). The echo time used was shorter compared with typical BOLD-fMRI acquisitions to allow for simultaneous BOLD-ASL recordings. The ASL data were collected for a different study and are not presented here. For all voxels, we computed the angle between the cortical surface and the external magnetic field of the scanner (θ_z) as described previously (Cohen-Adad et al., 2012; Fig. 5*D*). The BOLD changes versus θ_z for all voxels of the gray matter were binned at increments of 4° for θ_z and the plot is shown in Figure

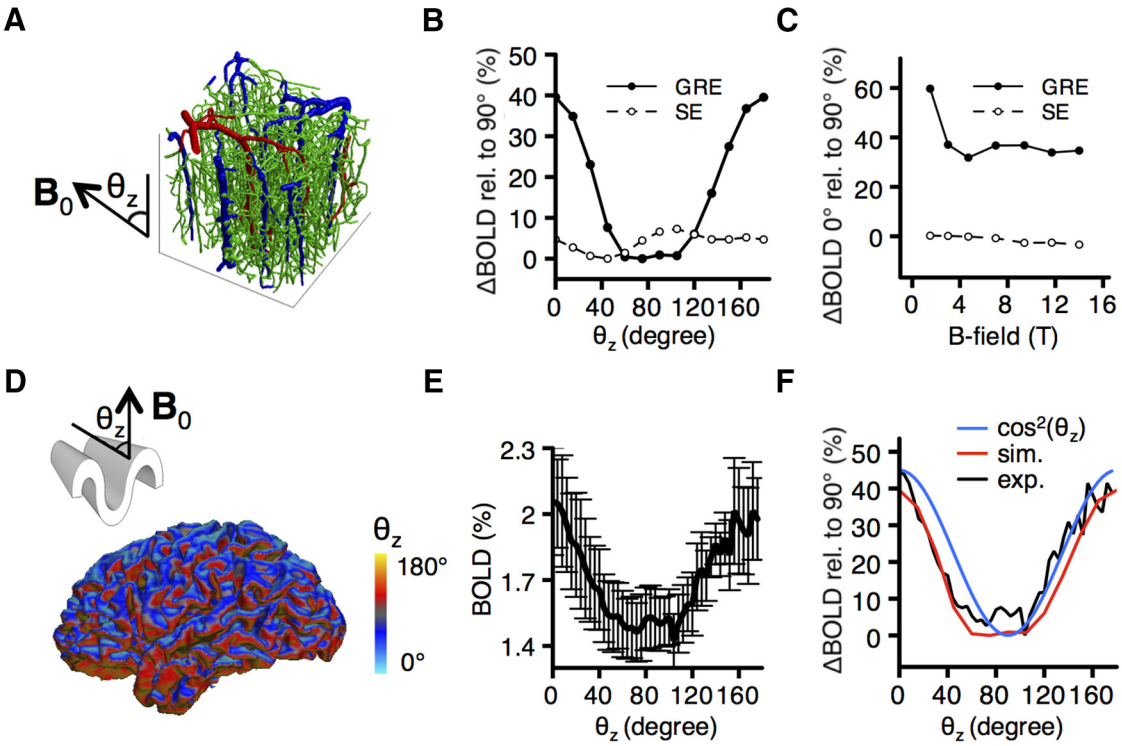

Figure 5. BOLD dependence on local folding of the cortex. ***A***, Convention for the angle (θ_z) between the vector normal to the local cortical surface and the external magnetic field (represented by the arrow). ***B***, Variation in the extravascular BOLD response at 3T predicted from simulations with θ_z ranging from 0° to 180° normalized by the BOLD response simulated for $\theta_z = 90°$. ***C***, Difference in the extravascular BOLD response simulated at $\theta_z = 0°$ relative to $\theta_z = 90°$ (in percentage relative to $\theta_z = 90°$) for different B-field strengths (TE = $T^*_{2,\text{tissue}}$). ***D***, Illustration of θ_z values computed in the gray matter of the human brain. ***E***, Averaged BOLD responses measured in the gray matter of human subjects during a hypercapnic challenge as a function of θ_z. ***F***, Comparison of angular dependence predicted from our simulations with angular dependence measured during the hypercapnic challenge in humans ($n = 5$ human subjects for experimental, $n = 6$ animals for simulations).

5*E*. The BOLD signal change produced by the hypercapnic challenge went from 1.5% at $\theta_z = 90°$ to 2.1% at $\theta_z = 0°$, and $\theta_z = 180°$ corresponding to a variation of 40%. Good agreements between simulations and experimental data were obtained for both the shape and the amplitude of this effect as shown in Figure 5*F*, confirming the predictive power of our bottom-up model. Variation in BOLD amplitude from 0 to 180° followed a shape similar to $\cos^2(\theta_z)$.

This spatial orientation dependence occurs because pial veins (which are the dominant sources of deoxyhemoglobin) are oriented parallel to the cortical surface (Fig. 6). As shown in Figure 6*A*, veins were mostly oriented either perpendicular to the cortical surface (ascending) or parallel to the cortical surface (pial) while the capillary bed had very little preferential orientation and was more uniform. However, the diameter of pial veins was generally larger compared with the diameter of ascending veins (Fig. 6*B*), as noted in previous studies (Blinder et al., 2013). Due to their larger diameter, pial veins were reflected more strongly in the BOLD signal compared with ascending veins, resulting in a $\cos^2(\theta_z)$ shape with stronger signal for $\theta_z = 0°$ compared with $\theta_z = 90°$ (Fig. 5*F*).

The angular dependence is exclusively extravascular since the intravascular BOLD signal should be totally isotropic. This is due to the random nature of red blood cell distribution (and magnetic field distortion) inside arteries and veins. Therefore, it is possible that the 60% variation predicted at 1.5T would be much weaker experimentally due to an important isotropic intravascular contribution at 1.5T (Boxerman et al., 1995a) not accounted by our simulations.

These results suggest that the same physiological change will produce BOLD responses with different amplitudes across the cortex depending on the spatial orientation with respect to B_0 of each specific voxel. This phenomenon can produce a confounding effect when comparing BOLD response from different subjects with different brain morphologies or with different spatial orientations of the head in the MRI scanner. More studies are needed to better characterize this phenomenon in human BOLD data including higher resolution data to quantify the variations of this effect at different cortical depths in humans. Nonetheless, the method used to map θ_z (Fig. 5*D*) can be used to correct for this confounding effect by introducing an additional regressor in the statistical analysis across different subjects with different orientations in the scanner, or different brain regions with different cortical orientations.

Reverse-engineering BOLD: quantifying contributions of individual vascular compartments and cerebral blood volume

The random diffusion of water molecules around the vasculature reduces the BOLD signal measured and this effect is more important for smaller vessels (Boxerman et al., 1995a). The contribution of smaller vessels is therefore reduced drastically, independently of their blood-volume fraction. This phenomenon limits our ability to accurately recover changes in $CMRO_2$ from calibrated BOLD data (Buxton, 2010; Griffeth and Buxton, 2011), unless a precise quantification of this effect is established. This quantification requires blood volume fraction, vessel diameter as well as the three-dimensional geometry of the vasculature for the arterial, venous, and capillary compartments. Although previous work has been limited to Monte Carlo simulation with straight cylinders and hypothetical values for vessel diameters and blood volume fraction (Uludağ et al., 2009), the bottom-up BOLD model presented

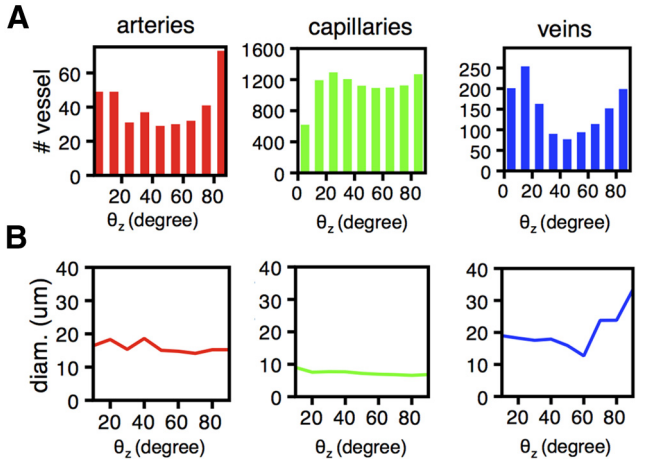

Figure 6. Statistics for vessel orientations and sizes. ***A***, Histogram of vessel orientation with respect to the *z*-axis for arteries, capillaries, and veins. ***B***, Mean vessel diameter as a function of vessel orientation with respect to the *z*-axis.

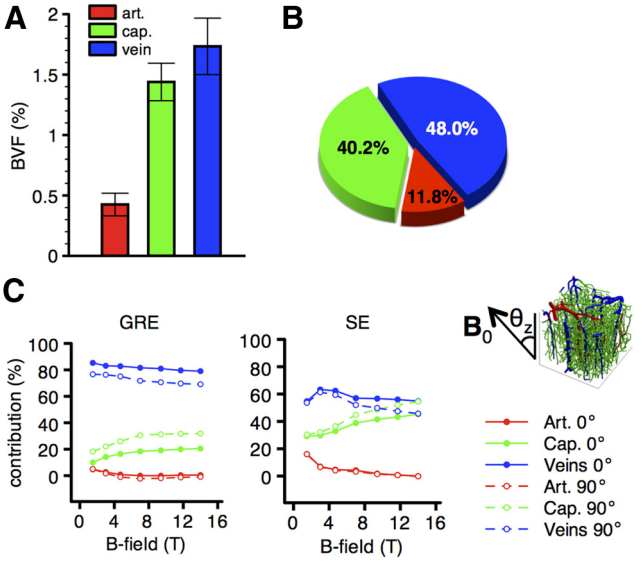

Figure 7. Compartment-specific contributions to the extravascular BOLD effect for different magnetic field strengths and cortical orientations. ***A***, Averaged blood volume fractions and (***B***) averaged vascular volume fractions for individual vascular compartments computed across the six VAN models. ***C***, Contributions of individual vascular compartment to the BOLD signal computed from the simulations ($n = 6$ animals).

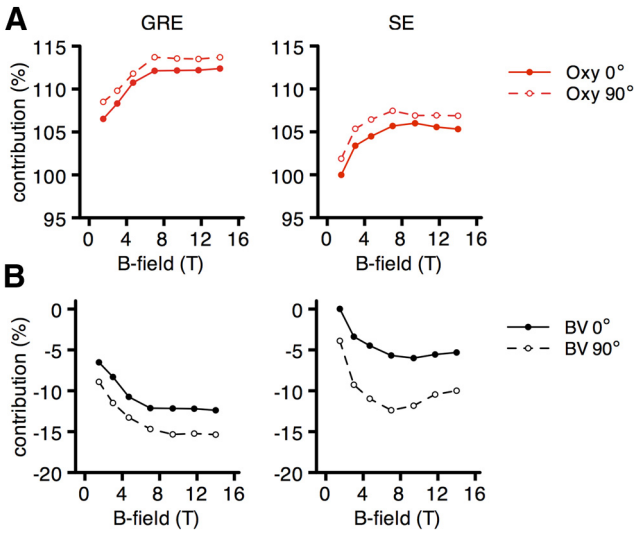

Figure 8. Independent contributions of (***A***) oxygenation changes and (***B***) blood volume changes to the extravascular BOLD signal for different magnetic field strengths and cortical orientations ($n = 6$ animals).

here provides an experimental measure of these three quantities and therefore allows us to compute the contribution of individual vascular compartments to the BOLD signal directly without any further assumption regarding these three parameters.

To quantify the effect of diffusion around smaller capillaries with high accuracy, we computed the blood volume fraction (Fig. 7*A*) and the vascular volume fraction (Fig. 7*B*) from the VAN models constructed from six animals. We then computed the individual contribution to BOLD of arteries, capillaries and veins for the six VAN models for B_0 ranging from 1.5 to 14T and for two cortical orientations with respect to B_0 (Fig. 7*C*). TE was set to $T_{2,\ tissue}^{*}$ for GRE and $T_{2,\ tissue}$ for SE (Table 3). Although the capillaries (defined as $R < 8\ \mu$m) account for 40% of the vascular volume (which is comparable to the vascular volume fraction of the veins, 48%), they only contribute to 10–30% of the GRE EV-BOLD signal. This lower contribution for capillaries is mainly due to diffusion effect. We also found that 75–85% of the GRE signal (depending on the cortical orientation) originate from oxygenation changes occurring in the veins at 1.5T and that this number decreases slightly with increasing B_0 to plateau at 70–80% at 14T. For clarity, the percentages reported above indicate the fraction of the signal arising from physiological changes occurring in the veins, and does not represent the fraction of voxels lying in veins. For SE, the 180° pulse refocuses the signal around larger vessels decreasing the venous contribution to 50% at 1.5T. Finally, the arterial contribution is negative for GRE as previously reported (Uludağ et al., 2009).

CBV changes are another important confounding factor in trying to recover changes in $CMRO_2$ from calibrated BOLD data (Buxton, 2010; Griffeth and Buxton, 2011) because the weighted average over all the vascular compartments containing deoxyhemoglobin is required to estimate the net CBV contribution. The beauty of the current model is that this net CBV contribution can be obtained directly without any further assumptions or complicated weighting and was therefore computed with our bottom-up model. The contribution of oxygenation changes are presented in Figure 8*A* and the net CBV contributions are presented in Figure 8*B* for both GRE and SE. The net CBV contributions are negative since an increase in vessel caliber increases the amount of deoxyhemoglobin present in a given voxel which decreases the signal measured. As an example, a net CBV contribution of −10% indicates that the BOLD signal would have been 10% larger if no blood volume change would have occurred. As mentioned above, the changes in venous volume used in our fMRI simulations were computed from the VAN models and not explicitly measured. Future studies will be required to establish the exact level of venous dilation during cerebral activation. In particular, recent work by Hall et al. (2014) provided new insights regarding the role of capillaries, whereas Huber et al. (2014) investigated CBV in positive and negative BOLD responses. Different venous dilation values would produce variations in the numbers given in Figure 8 but the net CBV contributions would remain negative as long as the veins are expanding.

Discussion

In this study, we aimed at constructing a validated bottom-up model of BOLD-fMRI by taking advantage of recent develop-

ment in quantitative two-photon microscopy of microvascular pO_2. Our modeling framework was validated against experimental data at several levels including the physiological and the biophysical level. Our model improved upon previous work by considering the real geometry of the microvasculature, as well as its real baseline deoxyhemoglobin distribution. The importance of this realism is twofold. First, our model provided a prediction of the magnitude of the effect of local cortical folding on the BOLD signal. It predicted signal variations up to 40% at 3T with TE = 13 ms. Taking into account this confounding effect in the analysis of BOLD data could significantly improve the quantification of fMRI in terms of physiological changes. The amplitude of the cortical-folding variations predicted from our model was further validated against experimental BOLD recordings on humans, demonstrating the predictive power of our model. Second, this realism allowed us to compute with high accuracy the contribution of individual compartment and the net blood volume contribution to the BOLD signal, two important confounding factors when estimating $CMRO_2$ changes from calibrated BOLD data, without having to assume blood volume fraction, vessel size, network geometry, or oxygen content of the individual vascular compartments.

As mentioned in Materials and Methods, an important assumption was necessary to model the physiological response to forepaw stimulation i.e., a coupling ratio for $\Delta Flow/\Delta CMRO_2$ of 3 was assumed. To validate this assumption, the simulated SO_2 changes were compared with experimental SO_2 changes and good agreement were obtained. Nevertheless, we performed a sensitivity analysis to test the impact of this assumption on the results reported in this manuscript. We varied the $\Delta Flow/\Delta CMRO_2$ coupling ratio from 2 to infinity (i.e., no changes in $CMRO_2$) in the VAN modeling and resimulated the BOLD response with each of the resulting SO_2 distributions. Although the amplitude of the BOLD response varied from 1 to 3% (which represents a variation of $\pm$50% compared with the 2% BOLD response obtained with a $\Delta Flow/\Delta CMRO_2$ coupling ratio of 3), neither the relative variations in the BOLD response produced by the local cortical folding nor the relative contributions of individual vascular compartments varied by >10% by varying the assumed $\Delta Flow/\Delta CMRO_2$ coupling ratio. This occurred because although the mean SO_2 change of the voxel varied with the $\Delta Flow/\Delta CMRO_2$ ratio, the relative SO2 changes between the different compartments were less variable. We also introduced 30% heterogeneity in the amplitude of the dilation traces used as inputs to the VAN to test the impact of heterogeneous dilation. Similarly, neither the relative variations in the BOLD response produced by the local cortical folding nor the relative contributions of individual vascular compartments varied by >5%. This occurred because heterogeneous dilation influenced the SO_2 distribution mostly in the arterial compartment and the first branches of the capillary compartment, which are not strongly represented in the BOLD response.

Although increasing the level of complexity can improve the predictive power of a model, as was the case here, this procedure often reduces its invertibility. A drawback of the complex bottom-up model presented here is that the high number of parameters and their non-uniqueness prevent the model to be inverted (i.e., one cannot recover oxygenation changes and vessel dilation in all compartments from a simple BOLD trace). Because an invertible BOLD model is required to recover $CMRO_2$ changes from flow and BOLD traces in the calibrated BOLD approach, researchers rely on the simplified top-down model originally proposed by Davis et al. (1998), which has never been validated against microscopic physiological measurements. By simulating macroscopic BOLD responses from different realistic physiological states, the detailed bottom-up model proposed here will provide a validated foundation to test and potentially improve the accuracy of the calibrated BOLD approach to recover $CMRO_2$ changes from combined flow and BOLD data.

The need for an accurate model describing the transformation of microscopic vascular dilation and oxygenation into macroscopic fMRI signals has increased recently with the development of magnetic resonance fingerprinting (MRF; Ma et al., 2013). In MRF, a pseudorandomized acquisition is used which causes the signals from different tissues to have a unique signal evolution termed "fingerprint". Following the acquisition, a pattern recognition algorithm is used to match the fingerprints to a predefined dictionary of predicted signal evolutions. This dictionary is constructed from an fMRI model predicting the macroscopic fMRI signal detected from the microscopic properties of the underlying tissue. Recently, MRF has been used to reconstruct blood oxygenation and blood volume simultaneously (Christen et al., 2014). The MRF dictionary used in this case was constructed from a Monte Carlo fMRI model with simplified vascular geometry and oxygen content. The bottom-up model presented here will provide a validated framework to validate and potentially improve this MRF dictionary by accounting for the real geometry and oxygenation of cortical microvasculature.

References

Attwell D, Buchan AM, Charpak S, Lauritzen M, Macvicar BA, Newman EA (2010) Glial and neuronal control of brain blood flow. Nature 468:232–243. CrossRef Medline

Banzett RB, Garcia RT, Moosavi SH (2000) Simple contrivance "clamps" end-tidal PCO(2) and PO(2) despite rapid changes in ventilation. J Appl Physiol 88:1597–1600. Medline

Blinder P, Shih AY, Rafie C, Kleinfeld D (2010) Topological basis for the robust distribution of blood to rodent neocortex. Proc Natl Acad Sci U S A 107:12670–12675. CrossRef Medline

Blinder P, Tsai PS, Kaufhold JP, Knutsen PM, Suhl H, Kleinfeld D (2013) The cortical angiome: an interconnected vascular network with noncolumnar patterns of blood flow. Nat Neurosci 16:889–897. CrossRef Medline

Boas DA, Jones SR, Devor A, Huppert TJ, Dale AM (2008) A vascular anatomical network model of the spatio-temporal response to brain activation. Neuroimage 40:1116–1129. CrossRef Medline

Boxerman JL, Bandettini PA, Kwong KK, Baker JR, Davis TL, Rosen BR, Weisskoff RM (1995a) The intravascular contribution to fMRI signal change: Monte Carlo modeling and diffusion-weighted studies in vivo. Magn Reson Med 34:4–10. CrossRef Medline

Boxerman JL, Hamberg LM, Rosen BR, Weisskoff RM (1995b) MR contrast due to intravascular magnetic susceptibility perturbations. Magn Reson Med 34:555–566. CrossRef Medline

Buxton RB (2010) Interpreting oxygenation-based neuroimaging signals: the importance and the challenge of understanding brain oxygen metabolism. Front Neuroenergetics 2:8. CrossRef Medline

Christen T, Zaharchuk G, Pannetier N, Serduc R, Joudiou N, Vial JC, Rémy C, Barbier EL (2011) Quantitative MR estimates of blood oxygenation based on T2*: A numerical study of the impact of model assumptions. Magn Reson Med 67:1458–1468. CrossRef Medline

Christen T, Pannetier NA, Ni WW, Qiu D, Moseley ME, Schuff N, Zaharchuk G (2014) MR vascular fingerprinting: a new approach to compute cerebral blood volume, mean vessel radius, and oxygenation maps in the human brain. Neuroimage 89:262–270. CrossRef Medline

Cohen-Adad J, Polimeni JR, Helmer KG, Benner T, McNab JA, Wald LL, Rosen BR, Mainero C (2012) T2* mapping and B0 orientation-dependence at 7T reveal cyto- and myeloarchitecture organization of the human cortex. Neuroimage 60:1006–1014. CrossRef Medline

Davis TL, Kwong KK, Weisskoff RM, Rosen BR (1998) Calibrated functional MRI: mapping the dynamics of oxidative metabolism. Proc Natl Acad Sci U S A 95:1834–1839. CrossRef Medline

Devor A, Sakadzic S, Saisan PA, Yaseen MA, Roussakis E, Srinivasan VJ, Vinogradov SA, Rosen BR, Buxton RB, Dale AM, Boas DA (2011) "Overshoot" of O_2 is required to maintain baseline tissue oxygenation at locations distal to blood vessels. J Neurosci 31:13676–13681. CrossRef Medline

Devor A, Tian P, Nishimura N, Teng IC, Hillman EM, Narayanan SN, Ulbert I, Boas DA, Kleinfeld D, Dale AM (2007) Suppressed neuronal activity and concurrent arteriolar vasoconstriction may explain negative blood oxygenation level-dependent signal. J Neurosci 27:4452–4459. CrossRef Medline

Devor A, Hillman EM, Tian P, Waeber C, Teng IC, Ruvinskaya L, Shalinsky MH, Zhu H, Haslinger RH, Narayanan SN, Ulbert I, Dunn AK, Lo EH, Rosen BR, Dale AM, Kleinfeld D, Boas DA (2008) Stimulus-induced changes in blood flow and 2-deoxyglucose uptake dissociate in ipsilateral somatosensory cortex. J Neurosci 28:14347–14357. CrossRef Medline

Drew PJ, Shih AY, Driscoll JD, Knutsen PM, Blinder P, Davalos D, Akassoglou K, Tsai PS, Kleinfeld D (2010) Chronic optical access through a polished and reinforced thinned skull. Nat Methods 7:981–984. CrossRef Medline

Drew PJ, Shih AY, Kleinfeld D (2011) Fluctuating and sensory-induced vasodynamics in rodent cortex extend arteriole capacity. Proc Natl Acad Sci U S A 108:8473–8478. CrossRef Medline

Dubeau S, Ferland G, Gaudreau P, Beaumont E, Lesage F (2011) Cerebrovascular hemodynamic correlates of aging in the Lou/c rat: a model of healthy aging. Neuroimage 56:1892–1901. CrossRef Medline

Fang QFQ, Boas DA (2009) Tetrahedral mesh generation from volumetric binary and grayscale images. Proc IEEE Int Symp Biomed Imaging 2009: 1142–1145.

Fang Q, Sakadzić S, Ruvinskaya L, Devor A, Dale AM, Boas DA (2008) Oxygen advection and diffusion in a three-dimensional vascular anatomical network. Opt Express 16:17530–17541. CrossRef Medline

Finikova OS, Lebedev AY, Aprelev A, Troxler T, Gao F, Garnacho C, Muro S, Hochstrasser RM, Vinogradov SA (2008) Oxygen microscopy by two-photon-excited phosphorescence. Chemphyschem 9:1673–1679. CrossRef Medline

Griffeth VE, Buxton RB (2011) A theoretical framework for estimating cerebral oxygen metabolism changes using the calibrated-BOLD method: modeling the effects of blood volume distribution, hematocrit, oxygen extraction fraction, and tissue signal properties on the BOLD signal. Neuroimage 58:198–212. CrossRef Medline

Hall CN, Reynell C, Gesslein B, Hamilton NB, Mishra A, Sutherland BA, O'Farrell FM, Buchan AM, Lauritzen M, Attwell D (2014) Capillary pericytes regulate cerebral blood flow in health and disease. Nature 508: 55–60. CrossRef Medline

Hillman EM, Devor A, Bouchard MB, Dunn AK, Krauss GW, Skoch J, Bacskai BJ, Dale AM, Boas DA (2007) Depth-resolved optical imaging and microscopy of vascular compartment dynamics during somatosensory stimulation. Neuroimage 35:89–104. CrossRef Medline

Hirsch S, Reichold J, Schneider M, Székely G, Weber B (2012) Topology and hemodynamics of the cortical cerebrovascular system. J Cereb Blood Flow Metab 32:952–967. CrossRef Medline

Huber L, Goense J, Kennerley AJ, Ivanov D, Krieger SN, Lepsien J, Trampel R, Turner R, Möller HE (2014) Investigation of the neurovascular coupling in positive and negative BOLD responses in human brain at 7T. Neuroimage 97:349–362. CrossRef Medline

Huppert TJ, Allen MS, Benav H, Jones PB, Boas DA (2007) A multicompartment vascular model for inferring baseline and functional changes in cerebral oxygen metabolism and arterial dilation. J Cereb Blood Flow Metab 27:1262–1279. CrossRef Medline

Kim SG, Ogawa S (2012) Biophysical and physiological origins of blood oxygenation level-dependent fMRI signals. J Cereb Blood Flow Metab 32:1188–1206. CrossRef Medline

Koch KM, Papademetris X, Rothman DL, de Graaf RA (2006) Rapid calculations of susceptibility-induced magnetostatic field perturbations for in vivo magnetic resonance. Phys Med Biol 51:6381–6402. CrossRef Medline

Kwong KK, Belliveau JW, Chesler DA, Goldberg IE, Weisskoff RM, Poncelet BP, Kennedy DN, Hoppel BE, Cohen MS, Turner R (1992) Dynamic magnetic resonance imaging of human brain activity during primary sensory stimulation. Proc Natl Acad Sci U S A 89:5675–5679. CrossRef Medline

Lecoq J, Parpaleix A, Roussakis E, Ducros M, Goulam Houssen Y, Vinogradov SA, Charpak S (2011) Simultaneous two-photon imaging of oxygen and blood flow in deep cerebral vessels. Nat Med 17:893–898. CrossRef Medline

Lindvere L, Janik R, Dorr A, Chartash D, Sahota B, Sled JG, Stefanovic B (2013) Cerebral microvascular network geometry changes in response to functional stimulation. Neuroimage 71:248–259. CrossRef Medline

Lipowsky HH (2005) Microvascular rheology and hemodynamics. Microcirculation 12:5–15. CrossRef Medline

Logothetis NK (2008) What we can do and what we cannot do with fMRI. Nature 453:869–878. CrossRef Medline

Lorthois S, Cassot F, Lauwers F (2011a) Simulation study of brain blood flow regulation by intracortical arterioles in an anatomically accurate large human vascular network. Part I: methodology and baseline flow. Neuroimage 54:1031–1042. CrossRef Medline

Lorthois S, Cassot F, Lauwers F (2011b) Simulation study of brain blood flow regulation by intracortical arterioles in an anatomically accurate large human vascular network. Part II: flow variations induced by global or localized modifications of arteriolar diameters. Neuroimage 54:2840–2853. CrossRef Medline

Ma D, Gulani V, Seiberlich N, Liu K, Sunshine JL, Duerk JL, Griswold MA (2013) Magnetic resonance fingerprinting. Nature 495:187–192. CrossRef Medline

Martindale J, Kennerley AJ, Johnston D, Zheng Y, Mayhew JE (2008) Theory and generalization of Monte Carlo models of the BOLD signal source. Magn Reson Med 59:607–618. CrossRef Medline

Nishimura N, Schaffer CB, Friedman B, Tsai PS, Lyden PD, Kleinfeld D (2006) Targeted insult to subsurface cortical blood vessels using ultrashort laser pulses: three models of stroke. Nat Methods 3:99–108. CrossRef Medline

Ogawa S, Lee TM, Kay AR, Tank DW (1990) Brain magnetic resonance imaging with contrast dependent on blood oxygenation. Proc Natl Acad Sci U S A 87:9868–9872. CrossRef Medline

Parpaleix A, Goulam Houssen Y, Charpak S (2013) Imaging local neuronal activity by monitoring PO2 transients in capillaries. Nat Med 19:241–246. CrossRef Medline

Pathak AP, Ward BD, Schmainda KM (2008) A novel technique for modeling susceptibility-based contrast mechanisms for arbitrary microvascular geometries: the finite perturber method. Neuroimage 40:1130–1143. CrossRef Medline

Pries AR, Secomb TW, Gaehtgens P, Gross JF (1990) Blood flow in microvascular networks: experiments and simulation. Circ Res 67:826–834. CrossRef Medline

Sakadzić S, Yuan S, Dilekoz E, Ruvinskaya S, Vinogradov SA, Ayata C, Boas DA (2009) Simultaneous imaging of cerebral partial pressure of oxygen and blood flow during functional activation and cortical spreading depression. Appl Opt 48:D169–D177. CrossRef Medline

Sakadzić S, Roussakis E, Yaseen MA, Mandeville ET, Srinivasan VJ, Arai K, Ruvinskaya S, Devor A, Lo EH, Vinogradov SA, Boas DA (2010) Two-photon high-resolution measurement of partial pressure of oxygen in cerebral vasculature and tissue. Nat Methods 7:755–759. CrossRef Medline

Sakadzić S, Mandeville ET, Gagnon L, Musacchia JJ, Yaseen MA, Yücel MA, Lefebvre J, Lesage F, Dale AM, Eikermann-Haerter K, Ayata C, Srinivasan VJ, Lo EH, Devor A, Boas DA (2014) Large arteriolar component of oxygen delivery implies a safe margin of oxygen supply to cerebral tissue. Nat Commun 5:5734. CrossRef Medline

Tian P, Teng IC, May LD, Kurz R, Lu K, Scadeng M, Hillman EM, De Crespigny AJ, D'Arceuil HE, Mandeville JB, Marota JJ, Rosen BR, Liu TT, Boas DA, Buxton RB, Dale AM, Devor A (2010) Cortical depth-specific microvascular dilation underlies laminar differences in blood oxygenation level-dependent functional MRI signal. Proc Natl Acad Sci U S A 107:15246–15251. CrossRef Medline

Tsai PS, Kaufhold JP, Blinder P, Friedman B, Drew PJ, Karten HJ, Lyden PD, Kleinfeld D (2009) Correlations of neuronal and microvascular densities in murine cortex revealed by direct counting and colocalization of nuclei and vessels. J Neurosci 29:14553–14570. CrossRef Medline

Turner R (2002) How much cortex can a vein drain? Downstream dilution of activation-related cerebral blood oxygenation changes. Neuroimage 16:1062–1067. CrossRef Medline

Uchida K, Reilly MP, Asakura T (1998) Molecular stability and function of mouse hemoglobins. Zoo Sci 15:703–706. CrossRef

Uludağ K, Müller-Bierl B, Uğurbil K (2009) An integrative model for neuronal activity-induced signal changes for gradient and spin echo functional imaging. Neuroimage 48:150–165. CrossRef Medline

Wehrl HF, Judenhofer MS, Maier FC, Martirosian P, Reischl G, Schick F, Pichler BJ (2010) Simultaneous assessment of perfusion with [15O] water PET and arterial spin labeling MR using a hybrid PET/MR device. Proc Intl Soc Mag Reson Med 18:715.

Wise RG, Ide K, Poulin MJ, Tracey I (2004) Resting fluctuations in arterial carbon dioxide induce significant low frequency variations in BOLD signal. Neuroimage 21:1652–1664. CrossRef Medline

Yablonskiy DA, Haacke EM (1994) Theory of NMR signal behavior in magnetically inhomogeneous tissues: the static dephasing regime. Magn Reson Med 32:749–763. CrossRef Medline

Yaseen MA, Srinivasan VJ, Sakadzić S, Radhakrishnan H, Gorczynska I, Wu W, Fujimoto JG, Boas DA (2011) Microvascular oxygen tension and flow measurements in rodent cerebral cortex during baseline conditions and functional activation. J Cereb Blood Flow Metab 31:1051–1063. CrossRef Medline

Yücel MA, Evans KC, Selb J, Huppert TJ, Boas DA, Gagnon L (2014) Validation of the hypercapnic calibrated fMRI method using DOT-fMRI fusion imaging. Neuroimage 102:729–735. CrossRef Medline

Zheng B, Lee PT, Golay X (2010) High-sensitivity cerebral perfusion mapping in mice by kbGRASE-FAIR at 9.4 T. NMR Biomed 23:1061–1070. CrossRef Medline